Journal of
Materials Chemistry A

Materials for energy and sustainability

Accepted Manuscript

This article can be cited before page numbers have been issued, to do this please use: C. G. Bezzu, B. Bartolomei, Y. Wu, M. Vaccaro, M. Longo, M. P. De Santo, A. Fuoco, M. Prato, M. Carta and J. Dosso, *J. Mater. Chem. A*, 2025, DOI: 10.1039/D5TA02477C.

ROYAL SOCIETY OF CHEMISTRY

rsc.li/materials-a

π-Extended Dihydrophenazine Based Redox Responsive Polymers of Intrinsic Microporosity

Received 00th January 20xx,
Accepted 00th January 20xx

DOI: 10.1039/x0xx00000x

Grazia C. Bezzu[a], Beatrice Bartolomei[b,c], Yue Wu[a], Martina Vaccaro[d], Mariagiulia Longo[d], Maria Penelope De Santo[e], Alessio Fuoco*[d], Maurizio Prato*[,b,f,g], Mariolino Carta* [a] and Jacopo Dosso*[b]

Redox-switchable Polymers of Intrinsic Microporosity (PIMs) are a promising yet underexplored class of materials. Here, we introduce π-extended dihydrophenazine-based PIMs for gas separation. The *tert*-butyl substituted **Phen-PIM-1** stands out as a rare redox-active switchable polymer example with a high surface area (BET >600 $m^2\ g^{-1}$) and excellent balance of porosity, pore size, and gas selectivity. **Phen-PIM-1** is soluble in N-methyl pyrrolidone (NMP), enabling membrane fabrication, while the methyl-substituted **Phen-PIM-2** is insoluble, highlighting the role of bulky *tert*-butyl groups in solubility and film formation. Gas separation studies, performed in powder (IAST), demonstrate outstanding performance, with a CO_2/N_2 selectivity up to 49. As a membrane material, **Phen-PIM-1** shows competitive separation within the Robeson upper bound for several commercially important gas pairs, proving its potential for carbon capture and molecular sieving. Furthermore, these materials exhibit efficient and reversible redox switching upon chemical stimuli, leading to marked differences in properties and enhanced selectivity. This study establishes dihydrophenazine-based PIMs as a versatile platform for developing tunable, high-performance membranes for energy and environmental applications.

1. Introduction

The development of novel porous polymeric materials is currently one of the most investigated areas of chemistry.[1,2] This interest rises from the great impact of such materials for applications in gas adsorption/separation,[1,3,4] energy storage,[5–8] and catalysis[9–12] which are of paramount importance to tackle the climate crisis that we are currently witnessing. As such, the number of works revolving around the development of innovative Metal organic frameworks (MOFs), Covalent organic frameworks (COFs) and in general, polymeric porous materials, is constantly rising. From this point of view, polymers of intrinsic microporosity (PIMs) have been extensively studied due to their highly promising surface areas and tunable functionalization, especially considering that many PIMs can be solution cast into membranes, thus they can be efficiently exploited for gas separation applications. From the structural point of view, PIMs are a class of highly porous materials defined by their rigid and contorted monomeric structures, which prevent efficient chain packing and create interconnected micropores (<2 nm). Their microporosity arises from a combination of intrinsic backbone rigidity and sites of contortion, such as spiro-centers or ladder-like linkages, that disrupt dense packing.[13] This results in high free volume and permanent porosity without the need for post-synthetic processing. PIMs' high surface area and tunable chemistry make them ideal for gas separation, CO_2 capture, and membranes.[14,15] Post-polymerization changes and further functionalization of the PIMs' backbones are extensively used strategies to improve their potential in gas separation and adsorption applications. For example, Weng[16] and co-workers exploited the nitrile groups present in pre-formed PIMs to generate triazine cross-links in situ, leading to improved separation performance despite a reduction in porosity. Similarly, Rizzuto et al.[17] demonstrated that reducing nitrile groups in PIM-1 to primary amines significantly enhanced CO_2 selectivity, attributing this effect to competitive sorption interactions confirmed via mixed-gas studies, solid-state NMR, and molecular dynamics, which showed chemical bonds between CO_2 and the amino-groups. Beyond gas separation, Song's[18] group engineered spirobifluorene-based PIMs to incorporate sulfonic acid in the repeat units, resulting in a significant improvement in redox flow battery performance. Building on this, stimuli-responsive structural modifications could further enhance PIMs selectivity and transport properties. In fact, despite a growing number of works reporting new types of PIMs with continuously improved properties, the concept of introducing responsive units in such materials is still underexplored, with most examples focusing on using light as stimulus.[4,19] Indeed, building PIMs functionalized with redox responsive molecular switches could produce materials that can change their properties "*on demand*". By employing chemical or electric stimuli these changes could lead to the tuning of their porosity, their polarity and charge, and their gas selectivity, all parameters that may greatly affect the final properties of a material.[14,15] Building on this idea, we recently reported the development and reversible molecular switching of symmetrically π-extended dihydrophenazines.[20,21] These molecules can be easily oxidized to their aromatic dicationic form, which is permanent once induced but can be reduced back to the neutral form by treatment with soft nucleophiles (e.g., Triphenylphosphine, Figure 1A). Moreover, the oxidation to the dicationic form is also associated with a dramatic electrochromic and conformational switch, which can have important effects when introduced in porous networks.[21] Given the rigidity and contortion of these molecules, which are typical

[a] Department of Chemistry, Faculty of Science and Engineering, Swansea University, Grove Building, Singleton Park, Swansea SA2 8PP, U.K.; [b] Department of Chemical and Pharmaceutical Sciences, CENMAT, Centre of Excellence for Nanostructured Materials, INSTM UdR Trieste, University of Trieste, via Licio Giorgieri 1, 34127 Trieste, Italy; [c] Department of Chemistry, Northwestern University, Evanston, Illinois 60208, United States; [d] Institute on Membrane Technology, National Research Council of Italy (CNR-ITM), via P. Bucci 17/C, Rende (CS) 87036, Italy; [e] Department of physics and CNR- Nanotec, university of Calabria, 87036 Rende, Italy [f] Centre for Cooperative Research in Biomaterials (CIC BiomaGUNE), Basque Research and Technology Alliance (BRTA), Paseo de Miramón 194, 20014, Donostia San Sebastián, Spain; [g] Basque Fdn Sci, Ikerbasque, 48013 Bilbao, Spain.

View Article Online
DOI: 10.1039/D5TA02477G

features of monomers that produce high performing PIMs,[22] and the relative ease of functionalization with catechol units (Figure 1B),[9] π-extended dihydrophenazines can be ideal candidates for the synthesis of redox switchable PIMs, especially exploiting nucleophilic aromatic substitutions as polymerization reaction, which is typical of polybenzodioxin-based PIMs[22] (Figure 1C).

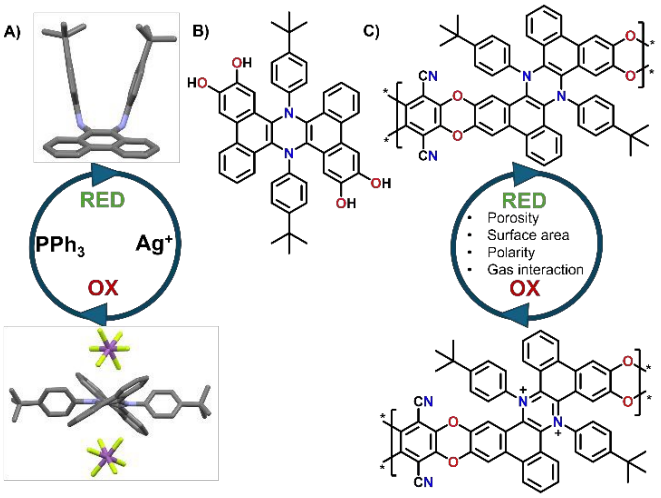

Figure 1. A) Parent π-extended dihydrophenazine chemical oxidation/reduction cycle, B) Catechol functionalized derivatives, C) Proposed structure of the switchable π-extended dihydrophenazine based PIMs.

As such, in this work we report the first synthesis and complete characterization of π-extended dihydrophenazine based PIMs. These materials present promising properties and can be reversibly oxidized and reduced, resulting in an increased selectivity between CO_2 and N_2 upon oxidation.

2. Results and Discussion

2.1. Synthesis of polymeric materials

Building on our previous work on π-extended dihydrophenazine systems,[20,21] we sought to utilize the presence of catechol moieties[9] and the rigid contorted nature of these backbones to synthesize polybenzodioxin-based polymers of intrinsic microporosity (PIMs). We deem this investigation as particularly significant because, as demonstrated in prior studies,[21] the dihydrophenazine backbone can be reversibly oxidized to its aromatic dicationic form, which leads to a conformational change that potentially could modify the microporosity of the material. In fact, based on a qualitative assessment of previously published XRD crystal structures (Figure 1A),[21] we believe this change results in a more rigid and contorted arrangement, characteristic of highly porous PIMs,[13] which may impact gas uptake, diffusion and release when used as a gas separation material. Herein we exploit this reversibility but within the polymeric chains, and not just on discreet molecules, to assess whether the expected changes also produce an alteration of the textural properties of the materials, such as porosity and pore size distribution (PSD). More specifically, we characterized the polymers in their initial pristine state (before oxidation, Figure 2A), after oxidation of the dihydrophenazine system (Figure 2B), and following its subsequent reduction to go back to the original form. In this way we aimed to confirm the polymers' ability to fully recover its initial properties, effectively demonstrating a chemo-switchable material. Building on previous findings about the irreversible structural changes in oxidized dihydrophenazine when exposed to nucleophilic molecules such as H_2O, we also investigated how this degradation occurs within the polymer (Figure 2C), aiming for a deeper understanding of the associated properties changes. This study is particularly focused on evaluating the potential of this chemo-switchable material for applications such as carbon capture and gas separation. In particular, any alterations in porosity and pore size distribution during oxidation-reduction cycles could significantly impact the permeability and selectivity of the polymers for commercially important gas pairs, especially CO_2/N_2. These insights are crucial for assessing their suitability in separation technologies.

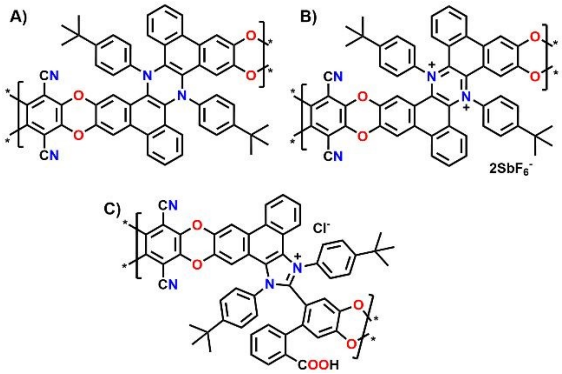

Figure 2. Structures of the three different versions of A) **Phen-PIM-1**, B) **Phen-PIM-1^{ox}**, C) **Phen-PIM-1^{deg}**.

We started the synthesis by preparing dihydrophenazine biscatechol **1** (Scheme 1) following a procedure reported in our previous contribution.[9] Since these substrates were never used in combination with tetrafluoroterephthalonitrile **5**, which is one of the most common fluorinated monomers used for the synthesis of PIMs, the reaction conditions were initially tested on **1** using an excess of **5** in presence of K_2CO_3 in anhydrous DMF at 60°C. As a result, the fluorinated monomeric unit **3** was obtained in a quantitative yield. Derivative **3** proved to be soluble enough in chlorinated solvents to be completely characterized using nuclear magnetic resonance spectroscopy (1D and 2D NMR). Moreover, the monomeric units presented a marked visible absorption in the 350-450 nm region of the spectra as typically associated with the introduction of oxygen atoms on the phthalonitrile system (Figure S31). The efficient preparation of model compound **3** confirmed that the same conditions would work in the polymerization and that the dihydrophenazine would not hinder it. Thus, **1** was treated with an equimolar amount of **5** in presence of K_2CO_3 in anhydrous and degassed DMF at 65°C for 70 h (Scheme 1). The long reaction time was used to ensure complete reaction of the starting materials, and the formation of long polymeric chains.[23] As a result, a dense bright yellow solid was formed, which was extensively purified by washing it with several solvents (section 2.6 in SI) to ensure removal of short oligomers and salts and

affording **Phen-PIM-1** as a dark yellow solid in almost quantitative yield.

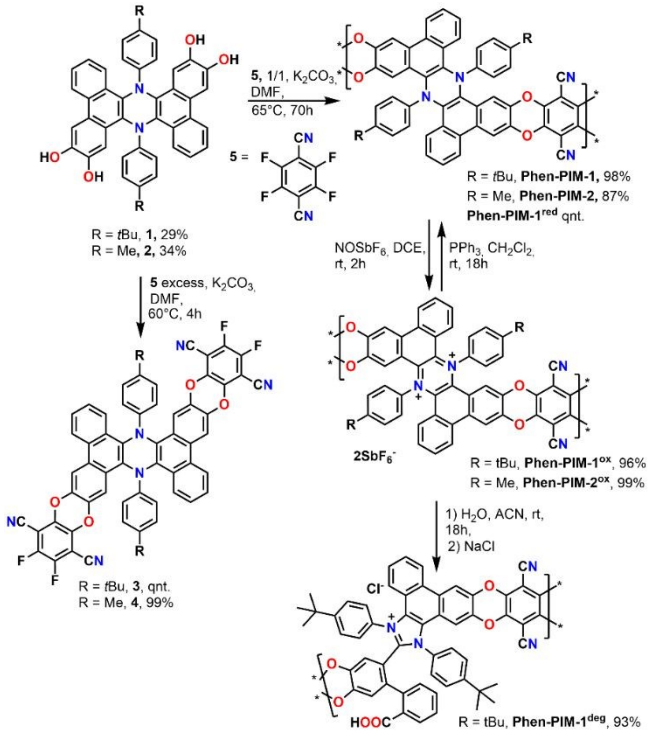

Scheme 1. Synthetic procedure for the preparation of dihydrophenazine models (**3** and **4**), **Phen-PIM-1** and **Phen-PIM-2** and their oxidation, reduction, degradation.

To assess the effects on the material properties of the *tert*-butyl group (*t*Bu), the same synthetic strategy was repeated with methyl functionalized dihydrophenazine **2**, resulting in the formation of **Phen-PIM-2**. We anticipated that the presence of the *t*Bu groups may slightly reduce the porosity compared to the methyl version, by a pore filling effect.[24] However, the larger aliphatic *t*Bu groups are also expected to enhance the solubility in organic solvents.[25] To test the feasibility of the oxidation reaction on the system, monomer **3** was treated with an excess of $NOSbF_6$ as oxidant, resulting in the formation of a deep green solution (Section 2.3 in SI). NMR analysis of the green solid highlighted the presence of a closed shell system fully consistent with the quantitative formation of dicationic $\mathbf{3^{2+}}$ (Figure S15-S17). Moreover, a UV-Vis investigation highlighted a profile also compatible with the formation of the dicationic system (Figure S31) in line with previously reported examples. Based on this, the same reaction was then carried out on the two polymers to generate their oxidized form. As such, **Phen-PIM-1** and **Phen-PIM-2** were suspended in dichloroethane (DCE) and treated with a slight excess of $NOSbF_6$ (Section 2.7 and 2.8 in SI). As a result, an immediate color change of the solids was visible and after purification $\mathbf{Phen\text{-}PIM\text{-}1^{ox}}$ and $\mathbf{Phen\text{-}PIM\text{-}2^{ox}}$ could be isolated in almost quantitative yield. To assess the reversible nature of the transformation, $\mathbf{Phen\text{-}PIM\text{-}1^{ox}}$ was then also treated with PPh_3 which is known to reversibly reduce the dicationic form to the initial neutral one, resulting in quantitative formation of $\mathbf{Phen\text{-}PIM\text{-}1^{red}}$. Finally, a batch of $\mathbf{Phen\text{-}PIM\text{-}1^{ox}}$ was also treated with H_2O in acetonitrile (ACN) solution, which, as expected based on previous reports by our group,[21] resulted in the irreversible degradation of the material generating $\mathbf{Phen\text{-}PIM\text{-}1^{deg}}$.

2.2. Characterization of PIMs

Structural assessment.

The thermal stability of the polymeric samples was assessed via thermogravimetric analysis (TGA, Figure S33). In addition, this technique allows the evaluation of the conversion of the pristine material into its oxidized form by monitoring the loss of the SbF_6^- counter-anion. In its completely oxidized form, $\mathbf{Phen\text{-}PIM\text{-}1^{ox}}$ (orange trace in Figure S33) contains approximately 35% of SbF_6^-. A step corresponding to a mass loss of ~28% with onset temperature of 250°C, which can be attributed to the loss of the counter-anion, can be readily observed as it is distinctly separated from the final decomposition step, which occurs at ~460°C similarly to that of the pristine material, allowing for clear identification of the oxidation product. Given the relative accuracy of this method, which involved a temperature increase ramp of 10°C min^{-1}, the experimental value indicates that 80% of the polymer backbone was successfully oxidized. Notably, the oxidized product could be effectively reverted to its original form (grey trace in Figure S33), as can be observed by its restored TGA curve which closely resembles that of the pristine material. Finally, the irreversible degradation into $\mathbf{Phen\text{-}PIM\text{-}1^{deg}}$ elucidated in our previous work,[21] was also confirmed as the theoretical loss of 4.1% corresponding to the mass of the chloride counter-anion, aligns closely with the ~5% step observed experimentally (purple trace in Figure S33).

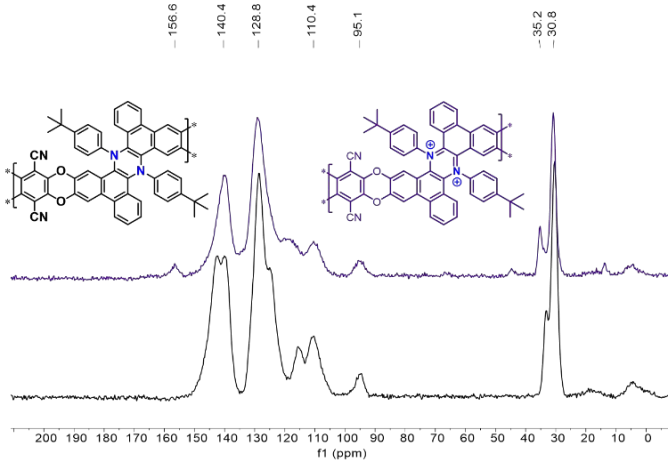

Figure 3. ^{13}C ssNMR of **Phen-PIM-1** (black trace) and $\mathbf{Phen\text{-}PIM\text{-}1^{ox}}$ (purple trace).

Due to the lack of solubility in common deuterated solvents, typically used for solution NMR, the **Phen-PIMs** structures were characterized by FT-IR (Figure S32) and ^{13}C solid-state -NMR (ssNMR, Figures S22-S27). In Figure 3, we display the ssNMR spectra of the two forms of **Phen-PIM-1**: the original (black trace) and the oxidized (purple), and we observe that all expected peaks are present and consistent with previously reported structures of similar phenazines. Although the two spectra appear rather similar, subtle differences are also

View Article Online
DOI: 10.1039/D5TA02477D

evident, suggesting that the transformation of the original **Phen-PIM-1** into its oxidized form has occurred.[21] Specifically, the peaks at ~30-33 ppm, which can be readily attributed to the *t*Bu substituents, in the oxidized form (purple) are slightly shifted to a lower field compared to the original (black). The signal at ~94 ppm, likely assigned to the carbon linked to the nitrile group, remains in the same position as it is distant from the nitrogen.[26] The aromatic region peaks are overlapped and difficult to assign precisely, but they are consistent with the reported structures, and the peaks at ~139-142 ppm show a slight shift and change in shape. Also, comparing the ^{13}C ssNMR of **Phen-PIM-1** and **Phen-PIM-1^{ox}** with the solution ^{13}C NMR of the monomeric units **3** and **3^{2+}** highlights an excellent correspondence between signals, suggesting the presence of very similar units in the materials. Finally, the presence of signals centered at 166.7 and 164.7 ppm in **Phen-PIM-1^{deg}**, which may be related to the COOH groups generated by the degradation (as confirmed by degradation of **3^{2+}**, see SI), are not observed in **Phen-PIM-1^{ox}**, which rules out the occurrence of extensive degradation in the latter and confirms the expected nature of the different polymers.

Textural and morphological characterization

Analysis of the samples by Scanning Electron Microscopy (SEM) revealed similar morphologies across all **Phen-PIM** samples (Figure 4), characterized by highly amorphous polymers with no discernible average dimensions. No significant differences were observed between the original and oxidized forms, indicating that particle size and morphology remain unchanged during the oxidation and reduction processes.

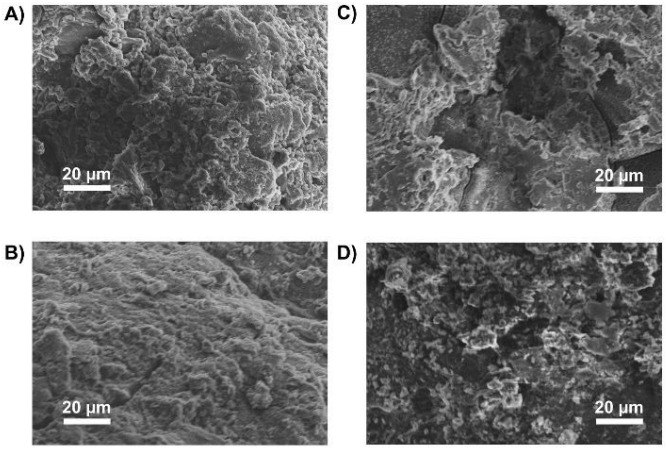

Figure 4. SEM images of the Phen-PIMs. A) **Phen-PIM-1** Pristine; B) **Phen-PIM-1$^{ox\text{-}red}$**; C) **Phen-PIM-1^{ox}**; D) **Phen-PIM-1^{deg}**.

As anticipated from the contorted structure of the monomers, both **Phen-PIM-1** (Figure 2A) and **Phen-PIM-2** exhibited the high porosity characteristic of high-performing PIMs.[22,23] The methyl functionalized polymer (**Phen-PIM-2**) proved to be only slightly more porous, with a SA_{BET} of 633 m^2 g^{-1}, compared to 618 m^2 g^{-1} for the *t*Bu version (**Phen-PIM-1**), as determined by nitrogen adsorption at 77 K. This was expected due to the pore filling effect of the *t*Bu group,[24] as already mentioned. Nevertheless, the difference is not particularly significant, which confirms that also **Phen-PIM-1** is highly microporous. Upon oxidation, both materials demonstrated a substantial reduction in porosity, likely due to the incorporation of the bulky SbF_6^- counter-anion, which is expected to occupy the pores and significantly reduce the initial free volume associated with the inefficient packing typical of PIMs, by generating an even more pronounced pore filling.[27] Because of that, the kinetics of nitrogen adsorption at 77 K proved to be significantly slow, resulting in negligible surface area measurements (Table 1). The pronounced hysteresis observed in the adsorption isotherms (see Figures S36-S37), however, indicated that the materials retained some degree of porosity, and suggests the presence of inaccessible or partially buried pores that are difficult for the relatively large N_2 probe gas to penetrate. To address this limitation, as reported in previous studies,[11] and to more properly assess the intrinsic porosity of these samples, carbon dioxide adsorption isothermal measurements at 273 K were performed. In fact, the smaller molecular size of CO_2 and the higher temperature of adsorption enhance diffusion and grant the access to smaller pores.[28] Indeed, these measurements confirmed that the oxidized PIMs remained porous, with surface areas of 244 m^2 g^{-1} for **Phen-PIM-2^{ox}** and 321 m^2 g^{-1} for the *t*Bu -functionalized polymer (**Phen-PIM-1^{ox}**, Figure 2B), calculated via the Grand Canonical Monte Carlo (GCMC) method.[28] Interestingly, in contrast to **Phen-PIM-2^{ox}**, in this case the *t*Bu-functionalized variant exhibited slightly higher porosity. As previously anticipated, **Phen-PIM-1** was also subjected to irreversible degradation, a process initially observed in the phenazine-backbone in the original study.[21] The resulting **Phen-PIM-1^{deg}** (Figure 2C), showed intermediate porosity, with a surface area of 246 m^2 g^{-1} calculated from the N_2 isotherm measured at 77 K, and 377 m^2 g^{-1} when evaluated with CO_2 at 273 K. This result aligns with expectations, as the chain rearrangements hinder efficient packing, and the counter-anion can be exchanged from SbF_6^- to the less bulky chloride counter-anion. Pore volume calculations, determined using both N_2 and CO_2 adsorption, confirmed that all polymers possessed substantial free volume, ranging from $7.460*10^{-2}$ to $5.620*10^{-1}$ cc g^{-1} (Table 1). A high free volume is obviously crucial for applications such as gas separation, as it will be discussed later. A key aspect of this study is represented by the reversibility of the porosity of the samples when subjected to oxidation and subsequent reduction, and this represents one of the most intriguing and distinctive properties of the new **Phen-PIMs**. As discussed, and shown in Figure S37, the oxidation of **Phen-PIM-1** leads to the expected decrease in adsorption and, consequently, in surface area. However, upon reduction, adsorption measurements revealed nearly identical isothermal curves and surface area calculations to those observed prior to oxidation (Figure 5A). This demonstrates that the porosity can be effectively restored, highlighting the material's ability to undergo cycles of oxidation and reduction while retaining its original performance.

View Article Online
DOI: 10.1039/D5TA02477C

Table 1. Textural properties of Phen-PIMs

Polymer	BET ($m^2 g^{-1}$)	Pore volume [a] ($cc\ g^{-1}$)	CO_2 adsorption 273 K (1 bar) ($cc\ g^{-1}$) ($mmol g^{-1}$)	CO_2 adsorption 298 K (1 bar) ($cc\ g^{-1}$) ($mmol g^{-1}$)	Selectivity [b] CO_2/N_2	Q_{st} [c] ($kJ\ mol^{-1}$)
This work						
Phen-PIM_2	633 (509) [a]	$4.473* 10^{-1}$	51 (2.28)	32 (1.41)	38	30.9
Phen-PIM_1	618 (501) [a]	$5.620* 10^{-1}$	55 (2.45)	38 (1.70)	49	29.1
Phen-PIM_2^{ox}	1.7 (244) [a]	$(7.460* 10^{-2})$ [a]	25 (1.12)	19 (0.85)	61	29.9
Phen-PIM_1^{ox}	1.05 (321) [a]	$(1.127* 10^{-1})$ [a]	32 (1.43)	21 (0.94)	64	32.2
Phen-PIM_1^{deg}	246 (377) [a]	$1.887* 10^{-1}$	43 (1.92)	26 (1.16)	42	32.9

[a] BET values from adsorption of N_2 at 77 K. In parentheses the surface areas calculated from CO_2 @273 K using the GCMC method.[28] [b] Selectivity calculated according to IAST at 298 K and 1 bar;[10,29] [c] Isosteric heat of adsorption (Q_{st} in kJ mol^{-1}) of corresponding gas at zero coverage calculated from isotherms collected at 273 and 298 K and fitted with the Langmuir-Freundlich equation and calculated via the Clausius Clapeyron equation.

The PSD of **Phen-PIMs** was assessed via CO_2 adsorption at 273 K, with calculations performed via the Non-Localized Density Functional Theory (NLDFT) method. The graph presented in Figure 5B reveals a PSD typical of PIMs,[30] featuring an initial set of peaks centered at 3-4 Å, corresponding to the ultra-microporous region, a broader range between 4.5-7 Å, and a final tail centered around 7-10 Å. The reduction in surface area following the oxidation of the **Phen-PIM** backbone is also reflected in the changes to the pore size distribution. Specifically, the peaks of the oxidized versions are significantly diminished (see Figure S39 for a full comparison), whereas the irreversibly modified polymer exhibits an intermediate PSD. Importantly, Figure 5B also demonstrates the complete reversibility of the PSD upon oxidation and subsequent reduction, as the two traces overlap almost perfectly.

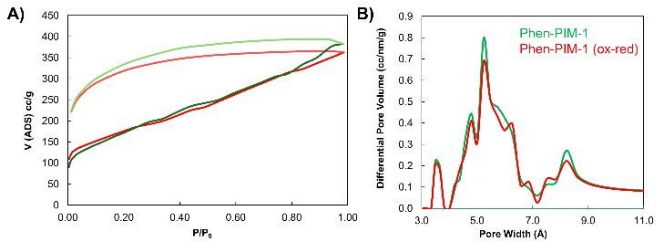

Figure 5. A) N_2 isotherms for **Phen-PIM-1** original (green) and after oxidation/reduction (red). The lighter curves represent the desorption pathway; B) Pore size distribution calculated from CO_2 adsorption at 273 K and via NLDFT. Color code original (green) vs oxidation/reduction (red).

CO_2 uptake, heats of adsorption and CO_2/N_2 IAST selectivity

All **Phen-PIMs** exhibited significant carbon dioxide uptake at both 273 K and 298 K (Table 1). The *t*Bu derivative showed slightly higher adsorption (2.45 mmol g^{-1} at 273 K and 1.70 mmol g^{-1} at 298 K) compared to the methyl counterpart (2.28 mmol g^{-1} at 273 K and 1.41 mmol g^{-1} at 298 K), although the values are very similar within the margin of error typical of these measurements. Despite the slightly lower surface area, we attribute the enhanced CO_2 uptake of the *t*Bu version to its higher amount of pores centered at ~4.5-7 Å, which we attribute to the narrowing of the pores size induced by the *t*Bu groups (Figure S40). The oxidized forms followed the same trend but exhibited lower overall uptake, likely due to the reduced porosity of the samples. Notably, despite the significant decrease in surface area upon oxidation, the CO_2 uptake remained relatively high (1.43 mmol g^{-1} at 273 K and 0.94 mmol g^{-1} at 298 K for **Phen-PIM-1^{ox}**), which shows good affinity for this gas. Consistent with the surface area trends, **Phen-PIM-1^{deg}** exhibited intermediate CO_2 uptake values, falling between those of the pristine and oxidized forms. Measurements of CO_2 adsorption at different temperatures also allowed for the calculation of the isosteric heats of adsorption (Q_{st}, Table 1 and Figure S41). Interestingly, all samples exhibited remarkably similar Q_{st} values (~30 kJ mol^{-1}), despite the expectation that the oxidized forms, with their permanent positive charge on the nitrogen atoms, would show a higher affinity for CO_2. This unexpected result suggests the existence of a trade-off between the increased electrostatic interactions provided by the charged nitrogen atoms, and the reduced surface areas of the oxidized samples. This balance appears to mitigate differences in adsorption behavior, resulting in comparable heats of adsorption across all samples and indicating a similar overall affinity for CO_2. Following the CO_2 adsorption measurements at 298 K, nitrogen adsorption was also conducted at the same temperature to evaluate the ideal selectivity of these materials for potential application in post-combustion separation processes.[31,32] Using the IAST++ software,[29] the adsorption curves were fitted with the IAST method to calculate the ideal selectivity, assuming a 15% CO_2 and 85% N_2 gas mixture, representative of typical flue gas compositions during post-combustion carbon capture.[33] The oxidized polymer achieved a selectivity exceeding 60, while the original **Phen-PIMs** afforded values ranging between 38 and 49. This can be attributed to the reduced pore size in the oxidized form that, despite allowing less CO_2 to pass through, block even more efficiently the larger N_2 molecules, thereby enhancing selectivity. As observed previously, the degraded sample exhibited intermediate performance, reinforcing the consistency of the system. It is worth noticing that, although the oxidized form demonstrated higher selectivity, its limited porosity makes the original polymer more practical for applications requiring the processing of larger gas volumes, as

View Article Online
DOI: 10.1039/D5TA02477C

Table 2. Single gas permeability P_a, diffusivity D_a, and solubility S_a, coefficients of gas, and associated selectivity over N_2 for methanol treated and 211 days aged films of **Phen-PIM-1** measured at 25°C and 1 bar of feed pressure.

Transport properties	Permeability, diffusivity and solubility					
	N_2	O_2	CO_2	CH_4	H_2	He
P_a [Barrer]	688.6	2628	12492	933.8	8254	3332
α (i/N_2)	(-)	(3.82)	(18.1)	(1.35)	(11.9)	(4.84)
Aged	356.8	1713	7994	470.6	6851	2868
α (i/N_2)	(-)	(4.80)	(22.4)	(1.31)	(19.2)	(8.04)
D_a [10^{-12} m^2 s^{-1}]	105.6	383.5	136.0	38.8	- [a]	- [a]
α (i/N_2)	(-)	(3.63)	(1.29)	(0.36)		
Aged	50.3	203	66.7	15.3	- [a]	- [a]
α (i/N_2)	(-)	(4.03)	(1.32)	(0.30)		
S_a [cm^3_{STP} cm^{-3} bar^{-1}]	4.89	5.14	68.9	18.0	- [a]	- [a]
α (i/N_2)	(-)	(1.05)	(14.1)	(3.68)		
Aged	5.32	6.31	89.9	23.0	- [a]	- [a]
α (i/N_2)	(-)	(1.19)	(16.9)	(4.32)		

[a] D_a and S_a values for H_2 and He are not reported due to the fast membrane time-lag

its higher flux capacity enables the treatment of greater amounts of gas simultaneously.

As anticipated, the presence of the *t*Bu groups had the effect of increasing polymer solubility. In fact, while **Phen-PIM-2** resulted poorly soluble in all solvents, **Phen-PIM-1** was soluble in *n*-methyl pyrrolidone (NMP), which allowed the casting of a robust film, suitable for the evaluation of its properties for potential applications as membranes for gas separation.

Moreover, it is worth mentioning that the limited solubility of the oxidized form, **Phen-PIM-1^{ox}**, prevented the formation of a stable film. As a result, the selectivity comparison between the two forms is based on the powder form using IAST calculations, as shown in Table 1. The pristine **Phen-PIM-1** film resulted insoluble in methanol, which could therefore be used for the standard soaking and drying treatment typically employed to remove traces of residual casting solvent from PIM films and to reverse the effect of physical aging. [34,35] Unfortunately, the scarce solubility of the methyl counterpart (**Phen-PIM-2**), prevented its gas permeability evaluation and, so, a full comparison of the two new PIMs. The order of gas permeability for **Phen-PIM-1** is $CO_2 > H_2 > He > O_2 > CH_4 > N_2$ (Table 2); that is half way between the trend of the ultra-permeable PIMs, in which CO_2 has a higher permeability than H_2,[25,36,37] and the typical trend of PIMs with very high diffusivity selectivity, in which He has a higher permeability than O_2.[38–40] The size-sieving character of **Phen-PIM-1** is highlighted by the steep correlation between the diffusion coefficient and the squared effective diameter of the gas with a slope increase for the aged film (Figure S43). The slope increase is usually associated to an increase of the Young's moduli of the film due to aging.[41] AFM force spectroscopy measurements were performed on both freshly methanol treated and aged samples in different positions, and the sampling scans shows that the freshly treated sample has a narrow distribution of the Young's modulus with average 1.79 ± 0.12 GPa (Figure S44A). Thus, this polymer proved to be stiffer with respect to PIM-1[42] but with similar Young's moduli or slightly more flexible than the ultrapermeable PIMs (Figure S44B).[37,41] The aged film shows a broader distribution, with two main peaks centered at 3.01 ± 0.16 GPa and 5.58 ± 0.32 GPa (Figure S44A). The aging trend is similar to what has been previously observed for other PIMs and the bimodal distribution can be associated to the fact that aging occurs predominantly at the surface of the film and this creates a concentration gradient of fractional free volume near the surface.[41,43]

The relative position of permeability and selectivity for selected gas pairs, which is displayed in the Robeson plot (Figure 6), serves as a critical tool for researchers and engineers to evaluate and compare the efficiency of new membrane materials in gas separation applications, such as carbon capture and natural gas purification. Developed by L.M. Robeson in 1991, revised in 2008 for most of the commercially important gas pairs and then updated by other groups for specific separations,[44–47] the plot depicts the performance of various polymeric membranes for gas separation, with permeability on the x-axis and selectivity (often represented as the ratio of the permeabilities of two gases) on the y-axis. In our case, the CO_2 permeability of **Phen-PIM-1** proved to be similar or higher than that of other *t*Bu containing PIMs (i.e., PIM-SBF-5,[40] PIM-TOT-SBF-5,[38] and DPt-TMPD[48]). Its higher selectivity, however, places this π-extended dihydrophenazine-based PIM above the 2008 upper bound in a more interesting region of the Robeson plots (Figure 6A and 6B), close to the requirements for high permeance/low-energy membranes for power plant post-combustion carbon dioxide capture foreseen by Merkel et al..[49] The high O_2/N_2 and He/N_2 selectivity (Figure 6C and 6D) is a further indication that the separation is strongly dependent on a molecular sieving mechanism, as both O_2 and especially He have a smaller kinetic diameter with respect to N_2 although their solubilities are not so different in polymers. In comparison with traditional low free volume polymers containing *t*Bu groups,[48,50–56] the **Phen-PIM-1** shows 2-3 orders of magnitude higher permeability values, while maintaining a similar

View Article Online
DOI: 10.1039/D5TA02477C

(CO_2/CH_4, O_2/N_2) or slightly lower (CO_2/N_2) selectivity (Figure 6), thus showing encouraging performance for gas separation application for biogas upgrading, CO_2 capture from flue gas and O_2/N_2 enrichment from air. In this work, we also investigated physical aging by repeating gas permeability experiments 211 days after the first measurements. Physical aging is a common phenomenon observed in highly microporous materials that are out of their thermodynamic equilibrium state, which in highly microporous polymers is characterized by the relaxation of the polymer's molecular chains, which leads to a reduction in internal free volume and, consequently, a decrease in permeability.[57] As shown in Figure 6, the expected loss of free volume resulted in a relative decrease in permeability for all gas pairs, accompanied by an increase in selectivity. Notably, the reduction in permeability is effectively counterbalanced by enhanced selectivity, ensuring that the overall performance remains relatively unchanged on the Robeson plot. This further demonstrates the enhanced molecular sieving effect achieved through the use of the dihydrophenazine monomer.

3. Conclusions

In this work, we have successfully demonstrated the potential of π-extended dihydrophenazine scaffolds as versatile building blocks for the development of novel microporous polymers. This study represents one of the few examples of structural redox-switchable PIMs reported in literature, further expanding the scope of functional materials in this class. Comprehensive characterization was carried out to assess the textural properties (surface area and pore size distribution), morphology (SEM), and chemical composition of the synthesized materials.

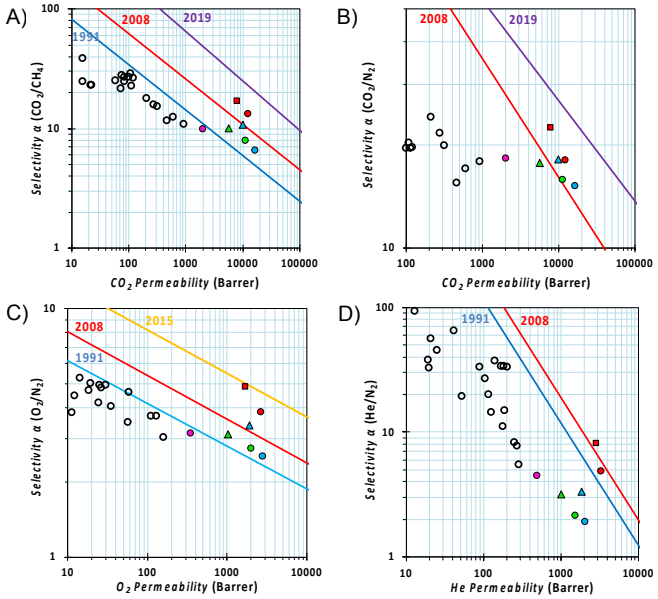

Figure 6. Robeson diagrams for the A) CO_2/CH_4, B) CO_2/N_2 C) O_2/N_2, and D) He/N_2 gas pairs with the upper bounds represented by blue lines for 1991,[44] red lines for 2008,[45] yellow lines for 2015,[47] and purple lines for 2019.[46] The gas permeabilities are reported for **Phen-PIM-1** in red (circle ● fresh and square ■ 211 days aged), for PIM-SBF-5 in blue (circle ● fresh and triangle ▲ 1439 days aged),[40] for PIM-TOT-SBF-5 in green (circle ● fresh and triangle ▲ 543 days aged),[38] for DPt-TMPD in pink (circle ● fresh),[48] and empty black circles are data for low free volume polymers with pendant *t*Bu groups.[48,50–56]

Our findings highlight a remarkable balance between porosity, pore size, and gas selectivity, making these materials highly promising for gas separation applications. The solubility of **Phen-PIM-1** in NMP enabled its processing into a self-standing membrane with mechanical properties in the range of other thin film forming materials, a crucial feature for practical implementation for gas separation. In contrast, the methyl-substituted counterpart **Phen-PIM-2**, exhibited poor solubility that prevented direct comparison of their membrane gas separation performance. These findings, although unfortunate, emphasize the critical role of large aliphatic *t*Bu groups in enhancing solubility and facilitating the formation of robust films. Gas separation studies, conducted both in powder form (via IAST) and in membrane form (via time-lag measurements), revealed excellent separation performance. Notably, **Phen-PIM-1** showed gas transport properties that place it in a highly competitive region of the Robeson upper bound for key gas pairs separations such as CO_2/CH_4 and CO_2/N_2, demonstrating its strong potential for carbon capture applications. Additionally, its performance in O_2/N_2 and He/N_2 separations suggests an enhanced molecular sieving effect, further broadening its applicability in gas purification processes.

Beyond its gas separation capabilities, this work marks an important milestone in the integration of dihydrophenazine-based compounds into the PIM family. The reversible redox behavior of these materials offers a rare example of switchable PIMs, opening new avenues for the design of stimuli-responsive porous materials. Given their highly promising properties, these materials lay a strong foundation for future optimization and functionalization, paving the way for their practical implementation in energy and environmental applications.

Author Contributions

The manuscript was written through contributions of all authors. All authors have given approval to the final version of the manuscript.

Conflict of Interest

The authors declare no conflict of interest.

Data Availability Statement

The data that support the findings of this study are available in the supplementary material of this article.

Acknowledgements

J. D. kindly acknowledges FRA2024-2025 funded by the University of Trieste and Microgrants 2024 funded by Regione FVG (LR 2/2011, ART. 4). M. P. is the AXA-Chair for Bionanotechnology (2016–2026). This work was supported by the University of Trieste, INSTM, and the Italian Ministry of Education MIUR (cofin Prot. 20228YFRNL). M.V. and A.F. received funding from the European Union's Horizon Europe research and innovation program under grant agreement no. 101115488, within the EIC pathfinder project "Double-Active

Membranes for a sustainable CO_2 - DAM4CO2" (HORIZON-EIC-2022-PATHFINDERCHALLENGES-01). C.G.B and M.C. gratefully acknowledge UK Research and Innovation (UKRI) under the UK government's Horizon Europe funding guarantee [grant number 10083164] associated with DAM4CO_2.
The authors kindly acknowledge Daniel M. Dawson and the University of St Andrews for the ^{13}C ssNMR service.

Notes and references

1 A. G. Slater and A. I. Cooper, *Science* , 2015, **348**, aaa8075-1.
2 T. D. Bennett, F. X. Coudert, S. L. James and A. I. Cooper, *Nat. Mater.*, 2021, **20**, 1179–1187.
3 Y. Li, J. Brückel, M. Jereb, A. Zupanc, S. P. Hirvonen, S. Hietala, M. Kemell, Y. Wu, O. Fuhr, R. D. Jansen-van Vuuren, M. Carta and S. Bräse, *Adv. Funct. Mater.*, 2024, **34**, 2401957.
4 A. Gafiullina, B. P. Ladewig and J. Zhang, *ACS Appl. Polym. Mater.*, 2023, **5**, 1–30.
5 J. Zhou and B. Wang, *Chem. Soc. Rev.*, 2017, **46**, 6927–6945.
6 X. Liu, C. F. Liu, W. Y. Lai and W. Huang, *Adv. Mater. Technol.*, 2020, **5**, 1–20.
7 J. Wu, F. Xu, S. Li, P. Ma, X. Zhang, Q. Liu, R. Fu and D. Wu, *Adv. Mater.*, 2019, **31**, 1–45.
8 J. Dosso, H. Oubaha, F. Fasano, S. Melinte, J.-F. Gohy, C. E. Hughes, K. D. M. Harris, N. Demitri, M. Abrami, M. Grassi and D. Bonifazi, *Chem. Mater.*, 2022, **34**, 10670–10680.
9 G. Gentile, B. Bartolomei, J. Dosso, N. Demitri, G. Filippini and M. Prato, *Chem. Commun.*, 2023, **60**, 602–605.
10 A. L. Myers and J. M. Prausnitz, *AlChE*, 1964, **11**, 121–127.
11 A. R. Antonangelo, N. Hawkins, E. Tocci, C. Muzzi, A. Fuoco and M. Carta, *J. Am. Chem. Soc.*, 2022, **144**, 15581–15594.
12 S. Mondal, A. Hassan, S. A. Wahed, A. Kumar and N. Das, *ACS Appl. Polym. Mater.*, 2025, 1503–1512.
13 N. B. McKeown, *Polymer* , 2020, **202**, 122736.
14 H. S. Lau, A. Eugenia, Y. Weng and W. F. Yong, *Prog. Mater. Sci.*, 2024, **145**, 101297.
15 H. W. H. Lai, F. M. Benedetti, J. M. Ahn, A. M. Robinson, Y. Wang, I. Pinnau, Z. P. Smith and Y. Xia, *Science* , 2022, **375**, 1390–1392.
16 W. Han, C. Zhang, M. Zhao, F. Yang, Y. Yang and Y. Weng, *J. Memb. Sci.*, 2021, **636**, 119544.
17 C. Rizzuto, Francesca Nardelli, Marcello Monteleone, L. Calucci, C. G. Bezzu, M. Carta, E. Tocci, E. Esposito, G. De Luca, B. Comesaña-Gándara, N. B. McKeown, B. Sayginer, P. M. Budd, J. C. Jansen and A. Fuoco, *J. Mater. Chem. A*, 2025, doi.org/10.1039/D4TA08839E.
18 C. Ye, A. Wang, C. Breakwell, R. Tan, C. Grazia Bezzu, E. Hunter-Sellars, D. R. Williams, N. P. Brandon, P. A. A. Klusener, A. R. Kucernak, K. E. Jelfs, N. B. McKeown and Q. Song, *Nat. Commun.*, 2022, **13**, 3184.
19 D. Becker, N. Konnertz, M. Böhning, J. Schmidt and A. Thomas, *Chem. Mater.*, 2016, **28**, 8523–8529.
20 J. Dosso and M. Prato, *Chem. - A Eur. J.*, 2023, **29**, e202203637.
21 J. Dosso, B. Bartolomei, N. Demitri, F. P. Cossío and M. Prato, *J. Am. Chem. Soc.*, 2022, **144**, 7295–7301.
22 N. B. McKeown, *Curr. Opin. Chem. Eng.*, 2022, **36**, 100785.
23 C. Pathak, A. Gogoi, A. Devi and S. Seth, *Chem. - A Eur. J.*, 2023, **29**, e202301512.
24 J. Jeromenok and J. Weber, *Langmuir*, 2013, **29**, 12982–12989.
25 I. Rose, C. G. Bezzu, M. Carta, B. Comesanã-Gándara, E. Lasseuguette, M. C. Ferrari, P. Bernardo, G. Clarizia, A. Fuoco, J. C. Jansen, K. E. Hart, T. P. Liyana-Arachchi, C. M. Colina and N. B. McKeown, *Nat. Mater.*, 2017, **16**, 932–937.
26 B. Satilmis, M. Lanč, A. Fuoco, C. Rizzuto, E. Tocci, P. Bernardo, G. Clarizia, E. Esposito, M. Monteleone, M. Dendisová, K. Friess, P. M. Budd and J. C. Jansen, *J. Memb. Sci.*, 2018, **555**, 483–496.
27 A. Wang, C. Breakwell, F. Foglia, R. Tan, L. Lovell, X. Wei, T. Wong, N. Meng, H. Li, A. Seel, M. Sarter, K. Smith, A. Alvarez-Fernandez, M. Furedi, S. Guldin, M. M. Britton, N. B. McKeown, K. E. Jelfs and Q. Song, *Nature*, 2024, **635**, 353–371.
28 D. Lozano-Castelló, D. Cazorla-Amorós and A. Linares-Solano, *Carbon* , 2004, **42**, 1233–1242.
29 S. Lee, J. H. Lee and J. Kim, *Korean J. Chem. Eng.*, 2018, **35**, 214–221.
30 M. Tian, S. Rochat, H. Fawcett, A. D. Burrows, C. R. Bowen and T. J. Mays, *Adsorption*, 2020, **26**, 1083–1091.
31 K. T. Leperi, R. Q. Snurr and F. You, *Ind. Eng. Chem. Res.*, 2016, **55**, 3338–3350.
32 R. Mobili, Y. Wu, C. X. Bezuidenhout, S. La Cognata, S. Bracco, M. Carta and V. Amendola, *RSC Sustain.*, 2024, 3345–3352.
33 H. Zhou, C. Rayer, A. R. Antonangelo, N. Hawkins and M. Carta, *ACS Appl. Mater. Interfaces*, 2022, **14**, 20997–21006.
34 P. M. Budd, N. B. McKeown, B. S. Ghanem, K. J. Msayib, D. Fritsch, L. Starannikova, N. Belov, O. Sanfirova, Y. Yampolskii and V. Shantarovich, *J. Memb. Sci.*, 2008, **325**, 851–860.
35 K. Nagai, A. Higuchi and T. Nakagawa, *J. Polym. Sci. Part B Polym. Phys.*, 1995, **33**, 289–298.
36 J. Chen, M. Longo, A. Fuoco, E. Esposito, M. Monteleone, B. Comesaña Gándara, J. Carolus Jansen and N. B. McKeown, *Angew. Chemie - Int. Ed.*, 2023, **62**, 1–9.
37 C. G. Bezzu, A. Fuoco, E. Esposito, M. Monteleone, M. Longo, J. C. Jansen, G. S. Nichol and N. B. McKeown, *Adv. Funct. Mater.*, 2021, **31**, 1–10.
38 S. A. Felemban, C. G. Bezzu, B. Comesaña-Gándara, J. C. Jansen, A. Fuoco, E. Esposito, M. Carta and N. B. McKeown, *J. Mater. Chem. A*, 2021, **9**, 2840–2849.
39 R. Malpass-Evans, I. Rose, A. Fuoco, P. Bernardo, G. Clarizia, N. B. McKeown, J. C. Jansen and M. Carta, *Membranes (Basel).*, 2020, **10**, 62–74.
40 C. G. Bezzu, M. Carta, M. C. Ferrari, J. C. Jansen, M. Monteleone, E. Esposito, A. Fuoco, K. Hart, T. P. Liyana-Arachchi, C. M. Colina and N. B. McKeown, *J. Mater. Chem. A*, 2018, **6**, 10507–10514.
41 M. Longo, M. P. De Santo, E. Esposito, A. Fuoco, M.

View Article Online
DOI: 10.1039/D5TA02477C

Monteleone, L. Giorno, B. Comesaña-Gándara, J. Chen, C. G. Bezzu, M. Carta, I. Rose, N. B. McKeown and J. C. Jansen, *Ind. Eng. Chem. Res.*, 2020, **59**, 5381–5391.

42 C. R. Mason, L. Maynard-Atem, N. M. Al-Harbi, P. M. Budd, P. Bernardo, F. Bazzarelli, G. Clarizia and J. C. Jansen, *Macromolecules*, 2011, **44**, 6471–6479.

43 B. W. Rowe, S. J. Pas, A. J. Hill, R. Suzuki, B. D. Freeman and D. R. Paul, *Polymer* , 2009, **50**, 6149–6156.

44 L. M. Robeson, *J. Memb. Sci.*, 1991, **62**, 165–185.

45 L. M. Robeson, *J. Memb. Sci.*, 2008, **320**, 390–400.

46 B. Comesaña-Gándara, J. Chen, C. G. Bezzu, M. Carta, I. Rose, M. C. Ferrari, E. Esposito, A. Fuoco, J. C. Jansen and N. B. McKeown, *Energy Environ. Sci.*, 2019, **12**, 2733–2740.

47 R. Swaidan, B. Ghanem and I. Pinnau, *ACS Macro Lett.*, 2015, **4**, 947–951.

48 R. Sulub-Sulub, M. I. Loría-Bastarrachea, H. Vázquez-Torres, J. L. Santiago-García and M. Aguilar-Vega, *J. Memb. Sci.*, 2018, **563**, 134–141.

49 T. C. Merkel, H. Lin, X. Wei and R. Baker, *J. Memb. Sci.*, 2010, **359**, 126–139.

50 Z. Qiu, G. Chen, Q. Zhang and S. Zhang, *Eur. Polym. J.*, 2007, **43**, 194–204.

51 N. Belov, R. Chatterjee, R. Nikiforov, V. Ryzhikh, S. Bisoi, A. G. Kumar, S. Banerjee and Y. Yampolskii, *Sep. Purif. Technol.*, 2019, **217**, 183–194.

52 S. Sánchez-García, F. A. Ruiz-Treviño, M. J. Aguilar-Vega and M. G. Zolotukhin, *Ind. Eng. Chem. Res.*, 2016, **55**, 7012–7020.

53 D. Ayala, A. E. Lozano, J. De Abajo, C. García-Perez, J. G. De La Campa, K. V. Peinemann, B. D. Freeman and R. Prabhakar, *J. Memb. Sci.*, 2003, **215**, 61–73.

54 N. Esteban, M. Juan-y-Seva, C. Aguilar-Lugo, J. A. Miguel, C. Staudt, J. G. de la Campa, C. Álvarez and Á. E. Lozano, *Polymers (Basel).*, 2022, **14**, 5517–5538.

55 M. Calle, Á. E. Lozano, J. G. De La Campa and J. De Abajo, *Macromolecules*, 2010, **43**, 2268–2275.

56 M. Calle, C. García, A. E. Lozano, J. G. De la Campa, J. De Abajo and C. Álvarez, *J. Memb. Sci.*, 2013, **434**, 121–129.

57 Z. X. Low, P. M. Budd, N. B. McKeown and D. A. Patterson, *Chem. Rev.*, 2018, **118**, 5871–5911.

The data supporting this article have been included as part of the Supplementary Information.

View Article Online
DOI: 10.1039/D5TA02477C